Check for updates

Journal of Biophotonics

JOURNAL OF BIOPHOTONICS

REVIEW

Tissue Mimicking Phantoms for Biomedical Optics: A Systematic Review of Inverse Adding–Doubling Characterization and Clinical Relevance

Elvis A. García-Cortés[1] | Luís M. Oliveira[2,3] | Julio C. Pérez-Sansalvador[1,4] | Teresita Spezzia-Mazzocco[1]

[1]Instituto Nacional de Astrofísica, Óptica y Electrónica (INAOE), Puebla, Mexico | [2]Institute for Systems and Computer Engineering, Technology and Science (INESC TEC), Porto, Portugal | [3]Physics Department, Polytechnic Institute of Porto – School of Engineering, Porto, Portugal | [4]Secretaría de Ciencia, Humanidades, Tecnología e Innovación (SECIHTI), Ciudad de México, Mexico

Correspondence: Teresita Spezzia-Mazzocco (terespezzia@inaoe.mx)

Received: 28 November 2025 | **Revised:** 19 February 2026 | **Accepted:** 19 March 2026

Keywords: biomedical engineering | imaging phantoms | near-infrared spectroscopy | optical coherence tomography | optical imaging | optical phenomena | radiation scattering

ABSTRACT

Tissue mimicking phantoms are essential for calibration and clinical translation of biophotonic techniques. Although the inverse adding–doubling (IAD) method is widely regarded as a reference standard for determining absorption and reduced scattering coefficients, significant inter-laboratory variability persists due to differences in integrating-sphere configurations, loss-compensation strategies, and model assumptions. This PRISMA-guided review (2015–2025) analyzes 10 experimental studies and proposes a unified comparison framework based on scattering power-law parameters (a, b) to relate phantom fabrication to clinically relevant optical targets. Nonlinear regression of continuous $\mu_s'(\lambda)$ spectra shows that selected PVC plastisol formulations reproduce dermal-like scattering slopes and that the power-law model provides consistent spectral descriptions ($\overline{R}^2 = 0.98$). By linking measurement methodology, spectral fitting, and mapping in (a, b) space, this work provides a practical framework to interpret variability and guide development of tissue-equivalent phantoms for reliable calibration of biophotonic devices.

1 | Introduction

Optical techniques have become indispensable in modern biomedical research and clinical care. Biophotonic modalities span a wide spectral range, extending from the ultraviolet all the way to the terahertz domain, and they support diverse diagnostic and therapeutic applications [1]. Techniques such as hyperspectral imaging (HSI), diffuse reflectance spectroscopy (DRS), optical coherence tomography (OCT), and photodynamic or laser therapies provide noninvasive access to physiological and structural information. However, their quantitative performance is strongly affected by the intrinsic heterogeneity of biological tissues, variability among patients, and differences in hardware design. These factors make it difficult to standardize measurements across laboratories and clinical environments, highlighting the need for robust reference materials that reproduce the optical behavior of biological tissue [2–6].

Tissue mimicking phantoms have therefore become essential tools for calibration, quality assurance, and validation of biophotonic systems. By providing stable and repeatable absorption and scattering conditions, these phantoms help bridge the gap between controlled laboratory measurements and their eventual use in clinical settings. Their application extends across a wide range of diagnostic and therapeutic contexts, including burn-depth assessment, tumor-margin delineation, studies of laser-tissue interactions, and quantitative oximetry [7–10]. In clinical specialties that increasingly rely on image

Abbreviations: DRS, diffuse reflectance spectroscopy; HSI, hyperspectral imaging; NIRS, near-infrared spectroscopy; OCT, optical coherence tomography.

© 2026 Wiley-VCH GmbH.

guidance, such as dermatology, oncology, and gastrointestinal endoscopy, phantoms enable continuous quality control of instruments whose diagnostic performance depends on precise optical calibration.

A broad spectrum of materials has been explored for phantom fabrication. Solid matrices such as polydimethylsiloxane (PDMS) [11–13], polyurethane [14, 15], silicone elastomers [8, 16], and PVC plastisol [17, 18] offer mechanical stability and long-term optical consistency, facilitating routine calibration in clinical and industrial settings. Hydrogels including agar [19–23], gelatin [24–26], and polyvinyl alcohol [27–29] better replicate the hydration and viscoelasticity of soft tissues, making them suitable for imaging and laser-therapy simulations. Tunable absorption is commonly achieved with India ink [13, 23, 30, 31], carbon black [11, 18, 32], hemoglobin [33–35], or nigrosin [19, 36], whereas scattering is controlled using titanium dioxide (TiO_2) [31, 37, 38], polystyrene microspheres [39, 40], or aluminum oxide (Al_2O_3) [9, 23]. More recent approaches employ intrinsic scattering generated by microcavities or refractive-index inclusions to improve homogeneity and reduce particle sedimentation [8].

Phantoms are typically classified as liquid, solid, or dynamic. Liquid formulations, often prepared with Intralipid and additional absorbers, are particularly useful for studies involving flow or oximetry [41–45]. Solid phantoms provide the stability needed for long term calibration and for standardizing measurements across different instruments [46, 47]. Dynamic and microfluidic phantoms can reproduce changes in perfusion, oxygenation, or time-dependent variations in scattering, which are essential for validating oximetry, perfusion monitoring, and laser therapy dosimetry [45, 47, 48].

Quantitative use of these phantoms requires accurate determination of the absorption coefficient (μ_a) and the reduced scattering coefficient (μ_s'). Among the available methods, the inverse adding–doubling (IAD) technique has become a reference standard for homogeneous turbid media, especially when implemented with single or double integrating spheres (IS). This combined IS-IAD approach is widely used due to its versatility [11, 49, 50]. Complementary approaches, such as spatial frequency domain imaging (SFDI) [51–54], time-resolved spectroscopy (TRS) [32, 55, 56], parameter retrieval based on OCT [57–59], Monte Carlo (MC) modeling [60–63], and inversions using diffusion theory [64], have broadened applicability to layered or heterogeneous tissues.

Clinically, phantoms translate optical principles into practice through models such as layered skin phantoms for laser parameter optimization or PDMS standards for assessing burn severity via OCT. Across these applications, the precise determination of $\mu_a(\lambda)$, $\mu_s'(\lambda)$, anisotropy $g(\lambda)$, and refractive index $n(\lambda)$ is a prerequisite for translating optical data into reliable diagnostic and therapeutic guidance. However, a critical challenge remains in the lack of inter-laboratory reproducibility when using the IAD method. Despite its theoretical status as a gold standard, discrepancies in experimental configurations, such as sphere geometry, port-to-sphere area ratios, loss-compensation strategies, and assumptions regarding g, often result in inconsistent findings for similar materials. These variations hinder the global standardization of biophotonic devices and underscore the need for structured comparative frameworks that enable objective cross-study analysis.

Within this context, this systematic review critically synthesizes advancements made between 2015 and 2025 in IAD-based characterization of tissue mimicking phantoms. Following PRISMA 2020 guidelines [65], we evaluate methodological variability and introduce a unified comparison framework based on power-law fitting of continuous reduced scattering spectra. This approach enables direct mapping of phantom-derived scattering parameters onto tissue optical databases. Our analysis indicates that while scattering amplitude primarily depends on particle concentration, certain matrices-particularly PVC plastisol-exhibit spectral slopes (b) comparable to those of dermal tissues, suggesting a practical pathway for the development of tissue-specific optical standards.

2 | Methods

This systematic review was conducted in accordance with the PRISMA 2020 guidelines [65]. Its objective was to identify and synthesize experimental studies published between 2015 and 2025 that used the IAD method to determine the μ_a and μ_s' of tissue-mimicking phantoms.

2.1 | Information Sources and Search Strategy

A comprehensive literature search was conducted on March 6, 2025 across six databases: PubMed, Scopus, Web of Science, IEEE Xplore, SPIE Digital Library, and OPTICA. The search strategy focused on high-level terms: "*tissue phantom*" OR "*tissue mimicking phantom*" AND "*optical properties*." Specifically, keywords such as "*integrating sphere*" and "*inverse adding doubling*" were not used as mandatory Boolean constraints during the initial search to maintain high sensitivity. This approach prevented the exclusion of relevant studies that emphasize phantom fabrication or clinical applications in their titles and abstracts while describing the IAD characterization exclusively within the methodology.

Due to export restrictions in the SPIE Digital Library, those records were manually collected by two independent reviewers to ensure completeness. All search results were exported in RIS format, merged, and de-duplicated using bibliographic software. The full search strings and Boolean operators for each database are provided in the Supporting Information.

2.2 | Eligibility Criteria

Studies were included if they met all the following criteria:

1. published in peer-reviewed journals between 2015 and 2025;
2. written in English;
3. reported fabrication or optical characterization of tissue mimicking phantoms for biomedical or biophotonic applications; and
4. explicitly determined both μ_a and μ_s' using the IAD method.

18640648, 2026, 4, Downloaded from https://onlinelibrary.wiley.com/doi/10.1002/jbio.70261 by Estsp Politecnico Do Porto, Wiley Online Library on [22/08/2026]. See the Terms and Conditions (https://onlinelibrary.wiley.com/terms-and-conditions) on Wiley Online Library for rules of use; OA articles are governed by the applicable Creative Commons License

The following types of publications were excluded: reviews, conference abstracts, theses, patents, preprints, non-English papers, and studies that characterized phantoms using methods other than IAD (e.g., SFDI, TRS, or Monte Carlo) without providing IAD-derived optical coefficients.

Eligible studies were grouped into four thematic domains to guide synthesis: (1) fabrication methods and materials, (2) measurement and analysis techniques, (3) reported optical properties, and (4) applications and objectives.

2.3 | Selection Process

Four reviewers independently screened all records in two stages: (1) title and abstract screening, followed by (2) full-text assessment for eligibility. Disagreements were resolved through consensus meetings. No automated screening tools or AI-based classifiers were used.

The complete PRISMA selection process, including identification, screening, eligibility assessment, and final inclusion, is summarized in Figure 1.

2.4 | Data Collection and Synthesis

Data extraction was performed by one reviewer and independently verified by three others. Extracted variables included:

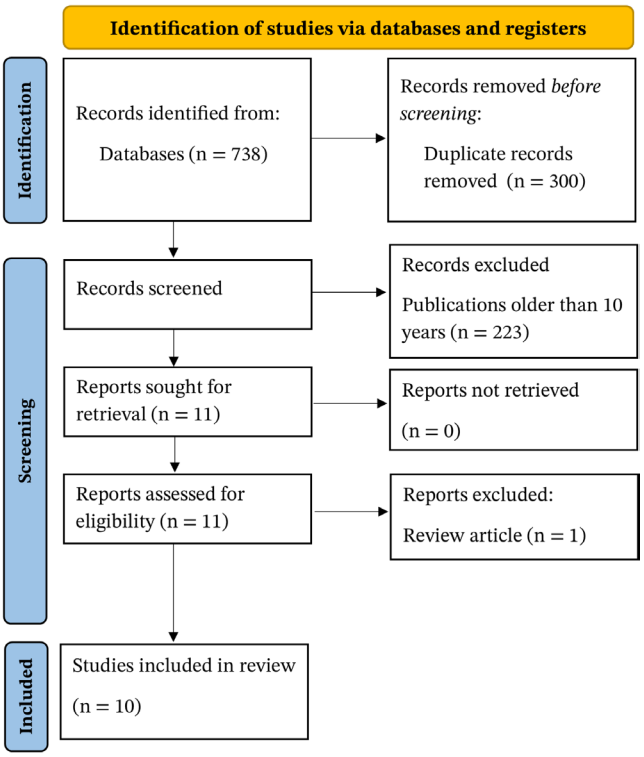

FIGURE 1 | PRISMA 2020 flow diagram summarizing the study identification and selection process. A total of 738 records were identified across six databases; 300 duplicates were removed, 438 titles and abstracts were screened, 11 full-text articles were evaluated, and 10 studies were included. Adapted from Page et al. [65] under CC BY 4.0.

1. phantom matrix composition (e.g., PDMS, agar, polyurethane, and PVC plastisol);
2. absorbing and scattering additives (e.g., carbon black, TiO_2, hemoglobin, and nigrosin);
3. fabrication protocol (mixing, degassing, curing, molding, or 3D printing);
4. measurement configuration (single or double integrating spheres, wavelength range, light source);
5. IAD analysis parameters (assumed or measured g, refractive index n, uncertainty analysis); and
6. reported optical coefficients (μ_a, μ_s', g) as functions of wavelength.

Optical coefficients were extracted directly from tables or text when available. When values were presented only in figures, numerical data were digitized using *WebPlotDigitizer*, and such points are noted as visually derived. Digitized values were used exclusively to reconstruct continuous $\mu_s'(\lambda)$ spectra; studies reporting only discrete μ_s' points were not interpolated nor included in power-law fitting. All data were converted to consistent units (cm^{-1}) for comparison across studies.

Extracted data were synthesized into four comparative tables summarizing:

- fabrication methods and materials (Table 1);
- measurement and analysis methods (Table 2);
- reported optical properties (Table 3); and
- intended biomedical applications (Table 5).

For the subset of studies reporting continuous reduced scattering spectra $\mu_s'(\lambda)$ [8, 11, 42, 67, 68], only these were eligible for power-law fitting. Other IAD-based studies either reported only discrete μ_s' values, did not report μ_s' at all, or provided normalized spectra that were unsuitable for wavelength dependent regression.

For eligible spectra, $\mu_s'(\lambda)$ was fitted to the power-law model

$$\mu_s'(\lambda) = a\left(\frac{\lambda}{500\ \text{nm}}\right)^{-b}, \tag{1}$$

using nonlinear least squares. Standard errors for a and b were obtained from the diagonal elements of the covariance matrix, and the coefficient of determination (R^2) was recorded for each fit. Fitted parameters and uncertainties are summarized in Table 4. Where applicable, phantom-derived (a, b) values were compared with literature-based tissue spectra, including epidermis and dermis from Kim et al. [67] and the broad tissue atlas of Jacques [69], as shown in Figure 2.

2.5 | Risk of Bias and Certainty Assessment

As this review synthesizes physical measurements rather than clinical outcomes, traditional clinical risk-of-bias tools were not applicable. Instead, methodological consistency, transparency of reporting, and completeness of optical characterization

18640648, 2026, 4, Downloaded from https://onlinelibrary.wiley.com/doi/10.1002/jbio.70261 by Estsp Politecnico Do Porto, Wiley Online Library on [22/08/2026]. See the Terms and Conditions (https://onlinelibrary.wiley.com/terms-and-conditions) on Wiley Online Library for rules of use; OA articles are governed by the applicable Creative Commons License

TABLE 1 | Fabrication materials, absorbing and scattering additives, and main preparation steps reported in the included phantom studies.

References	Matrix	Absorber	Scatterer	Fabrication technique	Type
Goldfain et al. [11]	PDMS	Carbon black (1–2 μm)	TiO_2 (0.3–1.0 μm), PS beads (~1 μm)	Suspension mixing, vacuum degassing, cured at RT then 75°C	Solid
Jang et al. [66]	PDMS	Human Hb (oxy/deoxy)	None	Sonicated, vacuumed, encapsulated Hb–PDMS, cured at RT	Solid
Kim et al. [67]	Gelatin–agar	Coffee powder[a]	TiO_2 (2%–10% w/v)	Sonicated, 3D-printed bilayer deposition, cured at RT	Solid
Kim et al. [19]	Agar (1.5%)	Nigrosin	Intralipid 20%	Microwave dissolved, mixed at ~50°C, poured, cooled	Solid
Lemaillet et al. (JBO) [7]	Polyurethane	Carbon black	TiO_2	Factory slabs (INO), molded, smooth surface	Solid
Lemaillet et al. (Appl. Opt.) [14]	Polyurethane	Carbon black	TiO_2	Molded slabs, reference-grade finish	Solid
Saager et al. [9]	PDMS (P-4)	None	Al_2O_3 (grit 400–1200)[b]	Manually mixed, vacuumed, cast sheets/blocks	Solid
Vincely and Vishwanath [42]	Water	Bovine Hb	PS spheres (1.0 μm)	Aqueous mixing, cuvette measurements	Liquid
Wróbel et al. [68]	PVC plastisol	Black ink (0.1%)	ZnO (340 nm)	Sonicated, degassed, molded, cured at 180°C	Solid
Wróbel et al. [8]	PDMS + glyc.	None	Intrinsic (glycerol cavities)[c]	Mixed, degassed, molded, cured at RT	Solid

[a]Coffee powder used as a melanin surrogate in layered skin phantoms.
[b]Grit size controls scattering magnitude and spectral slope.
[c]No exogenous scatterers added; glycerol-induced microcavities provide intrinsic scattering.

18640648, 2026, 4, Downloaded from https://onlinelibrary.wiley.com/doi/10.1002/jbio.70261 by Esasp Politecnico Do Porto, Wiley Online Library on [22/08/2026]. See the Terms and Conditions (https://onlinelibrary.wiley.com/terms-and-conditions) on Wiley Online Library for rules of use; OA articles are governed by the applicable Creative Commons License

TABLE 2 | Experimental configurations, IAD implementations, and correction or uncertainty procedures reported across the included studies.

References	Experimental setup	Analysis method	Corrections and uncertainty
Goldfain et al. [11]	Single integrating sphere; supercontinuum 400–700 nm; USB2000	IAD (fixed $g = 0.5$), iterative	Repeatability (5×), thickness, SRM reflectance, $n(\lambda)$ propagated
Jang et al. [66]	Dual-beam spectrophotometer with integrating sphere; VIS+NIR windows	Beer–Lambert (VIS μ_t); IAD for μ_a (NIR only)	Long-term stability (9–18 weeks) for oxy/deoxy Hb; no μ_s' retrieved
Kim et al. [67]	Double integrating spheres; halogen; OCT thickness	IAD (650–900 nm)	Colorimetry[a] (400–700 nm); human-skin comparison
Kim et al. [19]	Single sphere; supercontinuum + AOTF (FWHM 10 nm); 500 nm reference	IAD at 550 nm	Reflectance/transmittance normalization; non-scattered channel; saturation control
Lemaillet et al. (Appl. Opt.) [14]	Double spheres (UMBK-190); He–Ne 543.5/632.8 nm	IAD with calibrated sphere model	Full uncertainty budget[b]; $n = 1.521$, $g = 0.621$ from INO
Lemaillet et al. (JBO) [7]	Double spheres; polarization channel; reference detectors	IAD (modified); AD/IAD cross-check	Expanded uncertainty ($k = 2$) for μ_a, μ_s'; polarization test
Saager et al. [9]	Custom sphere; white-light 450–1000 nm	IAD with assumed $g = 0.8 - 0.9$	Multiple spatial positions; thickness control; g sensitivity low at $d \sim 1$ mm
Vincely and Vishwanath [42]	Single sphere (15.24 cm); halogen vs. supercontinuum	IAD + MC-correction/substitution[c]	Geometry MC; error maps; MAE 0.018 cm^{-1} (μ_a), 0.36 cm^{-1} (μ_s')
Wróbel et al. [68]	OL-750 with spheres; collimated T_c channel	IAD with R, T, T_c	OCT thickness; profilometry; RI fits $n(\lambda)$
Wróbel et al. [8]	OL-750; OCT; Abbe refractometry	IAD; retrieve μ_a, μ_s', g	Two-week repeatability; g from IAD (caveats discussed)

[a]Human skin comparison via colorimetry and OCT-derived thickness (bilayer epidermis/dermis).
[b]Uncertainty budgets include geometry, standards calibration, n, g, and alignment.
[c]MC-based correction or substitution used to compensate sphere losses; not applied simultaneously.

were assessed qualitatively following PRISMA 2020 recommendations [65]. Certainty of evidence was not graded, as the included studies focused on material properties rather than patient-level data.

3 | Results

3.1 | Study Selection

The initial database search yielded 738 records. After the removal of 300 duplicates, 438 unique records were screened by title and abstract. Of these, 223 were excluded for being published outside the inclusion period (before 2015) and 204 because they did not employ the IAD method for optical characterization. Eleven full-text articles were reviewed in detail; one was excluded for being a narrative review [70], resulting in 10 experimental studies for the final synthesis. The complete PRISMA 2020 flow diagram summarizing the identification, screening, and inclusion stages is shown in Figure 1.

3.2 | Study Characteristics

All 10 included studies (2015–2025) experimentally determined optical properties of tissue mimicking phantoms using the IAD method. The works covered solid, hydrogel, and liquid phantoms designed for calibration of optical devices, validation of imaging systems, and support of phototherapy and oximetry research. Fabrication protocols, measurement approaches, reported optical coefficients, and intended biomedical uses are summarized in Tables 1–5.

Across studies, reported optical windows spanned absorption coefficients of approximately $\mu_a \approx 0.01 - 4\ cm^{-1}$ and reduced scattering coefficients $\mu_s' \approx 0.1 - 86\ cm^{-1}$, with anisotropy factors g between 0.4 and 0.975. These ranges overlap with the optical regimes of skin, muscle, and mucosal tissues, supporting the use of these phantoms as tissue-relevant standards for diagnostic and therapeutic biophotonics.

3.3 | Fabrication Methods and Materials

The 10 studies employed a variety of matrices and additives to tailor absorption and scattering (Table 1). PDMS was the most frequently used matrix (four studies), chosen for its transparency, mechanical stability, and ease of molding. Goldfain et al. [11] independently tuned μ_a and μ_s' using carbon black and TiO_2 particles (0.3–1 μm), enabling systematic coverage of tissue-like optical regimes. Saager et al. [9] used aluminum-oxide grit of different sizes (400–1200) to control both the magnitude and

18640648, 2026, 4, Downloaded from https://onlinelibrary.wiley.com/doi/10.1002/jbio.70261 by Estsp Politecnico Do Porto, Wiley Online Library on [22/08/2026]. See the Terms and Conditions (https://onlinelibrary.wiley.com/terms-and-conditions) on Wiley Online Library for rules of use; OA articles are governed by the applicable Creative Commons License

TABLE 3 | Summary of reported absorption coefficients μ_a, reduced scattering coefficients μ_s', anisotropy factors g, spectral ranges, and main stability or validation checks for each included study.

References	μ_a (cm^{-1})	μ_s' (cm^{-1})	g	Spectral range	Stability/validation
Goldfain et al. [11]	0.10–1.45	0.10–44	0.5 (fixed)	500–850 nm	Repeatability; uncertainty propagation in IAD
Jang et al. [66]	oxyHb: 3.4 → 1.3; deoxyHb: 3.0 → 0.81	Not reported	n.r.	600–1000 nm	Hemoglobin stability (9–18 weeks)
Kim et al. [67]	Epidermis: 0.30 → 0.10; Dermis: 0.19 → 0.05	Epidermis: 2.3 → 1.0; Dermis: 2.5 → 1.2	n.r.	600–1000 nm	OCT-based layer thickness
Kim et al. [19]	1.26–2.13	1.20–2.17	n.r.	550 nm	Single-wavelength IAD at 550 nm
Lemaillet et al. [14]	0.01020–0.01203[a]	0.906–0.961	0.621 ± 0.015	543.5; 632.8	10 repeated measurements; NIST traceability
Lemaillet et al. [7]	0.0118–0.0120	0.90–1.03	0.621 ± 0.015	543.5; 632.8	Thickness series (5.08, 7.09, 9.92 mm)
Saager et al. [9]	0.00747–0.00816	0.730–0.982	0.8–0.9 (ass.)	400–1000 nm	Grit-dependent scattering
Vincely and Vishwanath [42]	SC: 0.86 → 0.096; HL: 0.97 → 0.10	SC: 23 → 18; HL: 19.3 → 14	0.9 (Mie)	500–800 nm	MC- or substitution-corrected IAD
Wróbel et al. [68]	Absorber: 0.16–0.41; None: 0.016–0.24	Absorber: 0.91–86.1[b]; None: 0.89–7.14	0.4–0.85	400–1100 nm	OCT thickness; $n(\lambda)$ fit
Wróbel et al. [8]	0.06–0.13	0.12–3.5	0.975 ± 0.01	500–1100 nm	Two-week temporal stability

[a]Range from the 10 repetitions reported for each wavelength.
[b]Upper bound corresponds to 8.61 mm^{-1} ≈86.1 cm^{-1}.

18640648, 2026, 4, Downloaded from https://onlinelibrary.wiley.com/doi/10.1002/jbio.70261 by Esasp Politecnico Do Porto, Wiley Online Library on [22/08/2026]. See the Terms and Conditions (https://onlinelibrary.wiley.com/terms-and-conditions) on Wiley Online Library for rules of use; OA articles are governed by the applicable Creative Commons License

TABLE 4 | Power-law parameters of the reduced scattering coefficient obtained from all continuous $\mu_s'(\lambda)$ spectra included in the analysis.

References	Sample/formulation	a (cm^{-1})	a_{err}	b	b_{err}	R^2
Goldfain et al. [11]	0.05–0.0025	6.684	0.0739	2.6267	0.0498	0.974
	0.05–0.0056	5.300	0.0832	3.0192	0.0815	0.958
	0.05–0.0200	5.805	0.0825	2.9300	0.0681	0.963
	0.10–0.0055	19.196	0.1561	1.7672	0.0316	0.975
	0.10–0.0201	19.492	0.1339	1.6745	0.0266	0.980
	0.11–0.0025	20.080	0.1452	1.7345	0.0306	0.979
	0.15–0.0025	29.870	0.2040	1.5451	0.0283	0.980
	0.15–0.0047	29.707	0.1927	1.6056	0.0251	0.980
	0.15–0.0125	30.463	0.1783	1.4864	0.0220	0.982
	0.15–0.0203	33.036	0.1796	1.4947	0.0203	0.985
	0.15–0.04	28.728	0.1513	1.4983	0.0200	0.985
	0.20–0.0201	46.263	0.2050	1.4244	0.0168	0.988
Kim et al. [67]	Epidermis phantom	39.800	0.9799	2.2327	0.0641	0.982
	Epidermis tissue	35.823	0.6425	1.9176	0.0458	0.987
	Dermis phantom	40.296	0.5242	1.9631	0.0333	0.993
	Dermis tissue	48.742	0.3756	2.1338	0.0199	0.998
Vincely and Vishwanath [42]	Corrected MC (HL)	17.788	0.0522	0.6573	0.0114	0.980
	Corrected MC (SC)	19.006	0.0390	0.5903	0.0076	0.985
Wróbel et al. [68]	A (200 μm)	3.654	0.0163	1.5290	0.0160	0.989
	B (200 μm)	30.184	0.0951	1.3956	0.0105	0.994
	A (500 μm)	4.178	0.0342	1.8090	0.0358	0.966
	B (500 μm)	3.934	0.0248	1.6242	0.0245	0.976
	A (1 mm)	4.486	0.0737	2.0356	0.0856	0.861
	B (1 mm)	3.405	0.0073	1.1432	0.0063	0.997
	A (1 mm)	3.215	0.0114	1.1339	0.0107	0.990
	B (1 mm)	4.486	0.0504	1.7246	0.0491	0.926
Wróbel et al. [8]	0.5 (v/v)	3.159	0.0329	1.1151	0.0250	0.987
	2 (v/v)	1.483	0.0083	0.7556	0.0133	0.991
	4 (v/v)	2.313	0.0077	0.5191	0.0074	0.994
	5 (v/v)	3.445	0.0092	0.3692	0.0059	0.993
	10 (v/v)	4.370	0.0097	0.4639	0.0049	0.997

Note: For each sample, the table reports the fitted amplitude a, spectral slope b, their standard errors, and the coefficient of determination R^2. Sample labels follow the notation of the original studies; for Goldfain et al. [11], "*x*–*y*" denotes TiO_2 and carbon-black concentrations (both in % w/w). Labels in Wróbel et al. [8, 68] (A/B and the thickness in parentheses) distinguish the phantom variants as reported by the authors.

spectral slope of scattering. Wróbel et al. [8] introduced glycerol-filled microcavities into PDMS to achieve highly forward-directed scattering ($g \approx 0.975$) without added particles.

Polyurethane-based phantoms [7, 14] provided mechanically robust slabs intended as reference standards for diffuse optics. Hydrogels based on agar or gelatin [19, 67] reproduced soft-tissue hydration and viscoelasticity and were used to construct layered skin-like models and gastrointestinal mimicking phantoms. PVC plastisol formulations [68] offered a low-cost, stable medium for OCT calibration. Liquid hemoglobin phantoms [42] enabled controlled studies of oximetry and flow, combining bovine hemoglobin with polystyrene spheres to provide physiologically relevant absorption and scattering.

Across all matrices, fabrication protocols typically involved homogenization of components, vacuum degassing to remove bubbles, casting into molds or cuvettes, and curing at room

18640648, 2026, 4, Downloaded from https://onlinelibrary.wiley.com/doi/10.1002/jbio.70261 by Estsp Politecnico Do Porto, Wiley Online Library on [22/08/2026]. See the Terms and Conditions (https://onlinelibrary.wiley.com/terms-and-conditions) on Wiley Online Library for rules of use; OA articles are governed by the applicable Creative Commons License

temperature or up to 80°C. The main materials, absorbers, scatterers, and preparation steps for each study are listed in Table 1.

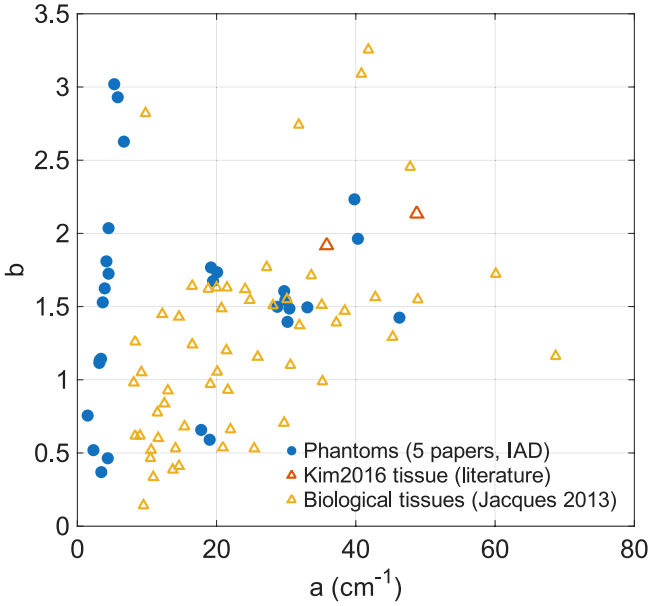

FIGURE 2 | Scatter plot of the power-law scattering parameters a and b for phantoms with continuous $\mu_s'(\lambda)$ spectra (five studies), shown together with reference tissue values from Jacques [69]. Phantoms cluster within tissue-like ranges of a and b, and the epidermis/dermis spectra from Kim et al. [67] appear in the expected region relative to other tissues.

3.4 | Measurement and Analysis Techniques

All 10 studies employed integrating sphere measurements combined with IAD analysis (Table 2). Single-sphere configurations were most common (six studies), while double-sphere setups [7, 14, 67] enabled simultaneous acquisition of reflectance and transmittance for improved accuracy. Light sources included broadband halogen lamps, He-Ne lasers, and supercontinuum sources, covering spectral ranges from approximately 400–1100 nm across the included studies.

MC or substitution-based corrections for sphere losses were explicitly implemented only in the single-sphere work of Vincely and Vishwanath [42], who reported reduced errors in both μ_a and μ_s'. The most detailed uncertainty analyses were provided in the NIST double-sphere studies [7, 14], where slab thickness, calibration standards, and sphere geometry were shown to dominate the error budget. Across all studies, anisotropy factors were either measured or assumed in the range $g = 0.5 - 0.975$, consistent with the microstructure of the scattering media (e.g., particle suspensions or glycerol microcavities).

3.5 | Reported Optical Properties

Across the 10 studies, IAD-derived optical coefficients covered the visible and near infrared windows between approximately 400 and 1100 nm. Absorption coefficients typically ranged from $\mu_a \approx 0.1 - 4\ \text{cm}^{-1}$, whereas reduced scattering coefficients spanned $\mu_s' \approx 0.1 - 86\ \text{cm}^{-1}$. Reported anisotropy

TABLE 5 | Intended applications of the phantoms and design features relevant to their specific biomedical or calibration uses.

References	Intended use	Design features tailored to application
Goldfain et al. [11]	Calibration of biomedical optical devices (HSI, DRS, NIRS, OCT)	Independent control of μ_a (carbon black) and μ_s' (TiO_2/PS); linear tunability vs. concentration
Jang et al. [66]	Oximetry, NIRS/HSI validation, PA imaging references	Oxy/deoxy Hb spectra embedded in PDMS; long-term stability; encapsulated geometry
Kim et al. [67]	Laser tattoo treatment planning; skin-tone emulation	Double-layer (epidermis/dermis); coffee as melanin surrogate; OCT-matched thickness
Kim et al. [19]	Technical evaluation of biomedical HSI; GI-like optical ranges at 550 nm	Agar + Intralipid + nigrosin; mandatory non-scattered channel for robust IAD
Lemaillet et al. (Appl. Opt.) [14]	Reference standards (NIST-traceable) for diffuse optics	Double-sphere with full uncertainty budget; stable polyurethane matrix
Lemaillet et al. (JBO) [7]	Measurement standards and inter-lab comparability	Polarization-insensitive DIS; validated AD/IAD; explicit n, g, θ
Saager et al. [9]	Instrument evaluation; pathology surrogates (burns/fibrosis)	Grit-controlled Al_2O_3 tunes μ_s' and spectral slope b; low-cost sheets
Vincely and Vishwanath [42]	Validation of single-sphere IAD; flow/oximetry phantoms	MC or substitution corrections; liquid Hb + PS at known g (Mie)
Wróbel et al. [68]	OCT calibration; skin-like optical window	PVC plastisol + ZnO + ink; controlled thickness, surface topography, and $n(\lambda)$
Wróbel et al. [8]	Optical clearing/porous-tissue emulation; flexible standards	PDMS-glycerol microcavities for intrinsic scattering; high g (~ 0.975)

18640648, 2026, 4, Downloaded from https://onlinelibrary.wiley.com/doi/10.1002/jbio.70261 by Estsp Politecnico Do Porto, Wiley Online Library on [22/08/2026]. See the Terms and Conditions (https://onlinelibrary.wiley.com/terms-and-conditions) on Wiley Online Library for rules of use; OA articles are governed by the applicable Creative Commons License

factors varied between $g \approx 0.4$ and 0.975, and refractive indices between $n \approx 1.33$ (aqueous media) and $n \approx 1.52$ (polyurethane). These global ranges match those observed for skin, muscle, mucosa, and other soft tissues in the wavelength range relevant for biophotonic diagnosis and therapy.

Table 3 summarizes the reported μ_a and μ_s' values, anisotropy factors, spectral ranges, and stability or validation checks for each study. In several cases, optical coefficients were not tabulated and were therefore reconstructed from published figures; these instances are indicated as visually estimated.

Beyond pointwise optical coefficients, five of the 10 studies reported continuous reduced-scattering spectra $\mu_s'(\lambda)$ suitable for power-law fitting [8, 11, 42, 67, 68]. Within this subset, the fitted amplitude a ranged approximately from 3 to 50 cm^{-1} and the spectral slope b from about 0.4–3 (Table 4). Most phantom formulations fell within scattering regimes characteristic of muscle, mucosa, and fibrous or dermal tissues.

Comparison with the tissue database compiled by Jacques [69] shows that several phantoms reproduce both tissue-like scattering slopes ($b \approx 1 - 1.7$) and amplitudes a for specific tissue classes. This is particularly evident for the epidermis/dermis phantoms of Kim et al. [67] and for selected PDMS and PVC plastisol formulations, which cluster near dermal and epithelial tissue classes in the (a, b) parameter space (Figure 2). The fitted power-law parameters and associated uncertainties are summarized in Table 4.

3.6 | Descriptive Analysis of Power-Law Parameters

To examine internal consistency within the extracted datasets, a descriptive statistical analysis was performed on the power-law parameters reported in Table 4. The scattering amplitude a showed substantial dispersion across formulations, reflecting differences in particle concentration, matrix composition, and intended optical targets.

In contrast, the spectral slope b exhibited matrix-dependent clustering. PVC plastisol phantoms showed a mean slope of $\overline{b} = 1.55 \pm 0.32$, closely corresponding to literature-reported dermal scattering slopes ($\overline{b} = 1.49 \pm 0.59$). Similarly, PDMS and gelatin–agar matrices yielded higher slopes ($\overline{b} = 1.90 \pm 0.59$ and $\overline{b} = 2.06 \pm 0.15$, respectively), consistent with more strongly wavelength-dependent scattering regimes reported for muscle and brain tissues.

Conversely, liquid hemoglobin phantoms and PDMS–glycerol formulations exhibited lower slopes ($\overline{b} \approx 0.64$), corresponding to weakly wavelength-dependent scattering typically associated with adipose or vascular-rich tissues.

The goodness-of-fit of the power-law model was assessed using the coefficient of determination. Approximately 90% of the continuous spectra yielded $R^2 > 0.95$, with a global mean of $\overline{R}^2 = 0.98$. Importantly, $\overline{R}^2$ quantifies only the agreement between the fitted model and the extracted $\mu_s'(\lambda)$ data. It does not represent metrological accuracy of the underlying integrating-sphere IAD measurements, which may still be affected by systematic biases related to sphere losses, port geometry, or assumed values of g and n.

3.7 | Applications and Objectives

The 10 studies addressed calibration, imaging, and therapeutic applications of tissue mimicking phantoms (Table 5). Lemaillet et al. [7, 14] reported polyurethane slabs characterized with double integrating spheres as reference standards for diffuse optics, supporting inter-laboratory comparability. Goldfain et al. [11] developed PDMS phantoms with independently tunable μ_a and μ_s' for general calibration of HSI, DRS, near-infrared spectroscopy (NIRS), and OCT systems. Kim et al. [19, 67] designed layered agar-gelatin or agar phantoms to emulate skin and gastrointestinal tissues, targeting laser-therapy optimization and HSI validation.

Jang et al. [66] introduced long-term stable hemoglobin phantoms for oximetry, NIRS, and photoacoustic imaging calibration. Vincely and Vishwanath [42] developed liquid phantoms with controlled flow and oxygenation, incorporating MC- or substitution-based corrections to validate single-sphere IAD implementations. Saager et al. [9] used grit-controlled scattering in PDMS to mimic changes in tissue microstructure associated with burns and fibrosis. Wróbel et al. [8, 68] provided PVC plastisol and PDMS-based standards for OCT calibration, skin-like optical windows, and studies of optical clearing in porous media.

Together, these applications highlight the translational value of optically characterized phantoms as a bridge between laboratory calibration and clinical practice. By providing reproducible, tissue-like optical conditions for skin, mucosa, vascular, and parenchymal tissues, IAD-based phantoms support the validation of diagnostic imaging systems, the optimization of laser-therapy dosimetry, and the quantitative assessment of optical biomarkers in oncology, dermatology, and other clinically relevant fields.

4 | Discussion

This systematic review summarizes experimental work from 2015 to 2025 on tissue mimicking phantoms characterized using the IAD method. Across the 10 included studies, optical phantoms were fabricated using diverse matrices and characterized primarily in the visible and NIR ranges. The discussion below interprets the main findings, evaluates methodological performance, and outlines clinical implications.

4.1 | General Interpretation of Findings

The reviewed studies demonstrate that IAD enables consistent retrieval of absorption and reduced scattering coefficients within the optical regimes of many clinically relevant tissues. The global ranges in Table 3 ($\mu_a \approx 0.01 - 4$ cm^{-1}, $\mu_s' \approx 0.1 - 86$ cm^{-1}) are compatible with reported values for epidermis, dermis, muscle, and mucosa. Within these ranges, PDMS and polyurethane

18640648, 2026, 4, Downloaded from https://onlinelibrary.wiley.com/doi/10.1002/jbio.70261 by Estsp Politecnico Do Porto, Wiley Online Library on [22/08/2026]. See the Terms and Conditions (https://onlinelibrary.wiley.com/terms-and-conditions) on Wiley Online Library for rules of use; OA articles are governed by the applicable Creative Commons License

matrices serve as robust scattering-dominated reference phantoms, whereas agar, gelatin, and PVC plastisol more readily achieve the higher μ_a values characteristic of pigmented or hemoglobin-rich tissues.

Beyond pointwise coefficients, the power-law analysis of $\mu_s'(\lambda)$ provides a compact description of tissue-like scattering behavior. Comparison with the Jacques atlas [69] clarifies how specific phantoms map onto biological classes: highly scattering PDMS–TiO_2 formulations overlap with epithelial tumors, while liquid hemoglobin phantoms align with weakly scattering parenchymal tissues. In this sense, the power-law parameters in Table 4 provide a quantitative link between phantom design and specific biological targets. However, the reliability of this link depends heavily on the precision of the underlying measurements.

4.2 | Measurement Performance and Methodological Heterogeneity

To interpret the variability in reported optical properties, we examined methodological differences across the included studies. A major contributor is the integrating-sphere configuration and the strategy used to account for sphere losses. Studies employing double integrating spheres, such as those by Lemaillet et al. [7, 14], reported comparatively lower expanded uncertainties, largely due to the simultaneous acquisition of diffuse reflectance and transmittance, which reduces sensitivity to sample repositioning and source fluctuations.

In contrast, single-sphere configurations require careful modeling of port losses and internal sphere geometry. If not explicitly compensated, these effects can introduce systematic underestimation of μ_a and μ_s'. Vincely and Vishwanath [42] demonstrated that Monte Carlo-based corrections can substantially reduce such biases, achieving mean absolute errors below 5% under controlled conditions.

Across the reviewed literature, however, the level of detail provided regarding sphere geometry, port-to-sphere area ratios, and uncertainty propagation varied considerably. These differences in reporting and compensation strategies likely contribute to the dispersion of optical coefficients summarized in Table 3. This observation does not invalidate individual studies; rather, it highlights the need for more standardized documentation of IS–IAD implementation parameters to improve inter-laboratory comparability.

4.3 | Methodological Limitations and Uncertainty

Beyond measurement geometry, additional variability arises from fabrication practices and the assumptions of the power-law model. Differences in light sources, curing conditions, and sample thickness affect the derived coefficients, and incomplete reporting of these parameters in some works limits reproducibility.

The power-law analysis itself introduces sensitivity to the chosen wavelength normalization and fitting window. Studies restricted to narrow bands (e.g., 650–900 nm) will yield different slopes from those spanning 400–1100 nm. Furthermore, as some datasets were digitized from figures, systematic errors may exist despite high R^2 values. Consequently, the overlap between phantoms and tissues in Figure 2 should be interpreted as semi-quantitative, demonstrating that current phantoms reach tissue-like regimes while acknowledging that small discrepancies in slope remain.

4.4 | Clinical and Biomedical Relevance

The optical-property ranges achieved by the reviewed phantoms correspond well to those found in human tissues, making them directly applicable to biomedical imaging and therapy validation. PDMS and polyurethane standards have been used for the calibration of integrating sphere systems, diffuse reflectance spectroscopy, and OCT, where accurate μ_a and μ_s' are needed to interpret tissue structure and pathology.

Our descriptive analysis in Section 3.6 further refines this perspective by identifying matrix formulations whose scattering slopes (b) closely approximate those reported for specific tissue classes (e.g., PVC plastisol for dermal-like scattering behavior). This spectral correspondence provides a rational basis for selecting phantom compositions according to the intended clinical application.

IAD-characterized phantoms are critical for calibrating OCT, HSI, and NIRS systems, but their practical utility depends on transparent documentation. Practitioners should prioritize phantoms with publicly available recipes and comprehensive uncertainty budgets, ideally traceable to NIST or ISO standards [7, 14, 49]. Due to the relevance of the tissue optical clearing method [71], and its significance in creating transparency for acquiring diagnostic data, the standardization of phantom preparation is a significant step forward. This allows for the quantification of broadband optical properties in healthy and diseased tissues, providing essential knowledge regarding induced transparency prior to clinical use in patients.

The "design map" provides a practical framework for researchers. For instance, phantoms clustering near dermal reference points are natural candidates for calibrating devices aimed at fibrosis staging or burn-depth assessment. Similarly, hemoglobin-based phantoms developed for oximetry and photoacoustic studies reproduce realistic absorption peaks, bridging the gap between laboratory standards and clinical diagnostics.

4.5 | Future Directions

Future work should prioritize the development of standardized measurement and reporting protocols to reduce the inter-laboratory variability identified in this review. In particular, harmonized documentation of integrating-sphere geometry, loss compensation strategies, and IAD input parameters would substantially improve reproducibility. Although the studies summarized in Table 2 primarily addressed the visible and near-infrared ranges, future investigations should extend phantom validation across broader spectral domains.

18640648, 2026, 4, Downloaded from https://onlinelibrary.wiley.com/doi/10.1002/jbio.70261 by Estsp Politecnico Do Porto, Wiley Online Library on [22/08/2026]. See the Terms and Conditions (https://onlinelibrary.wiley.com/terms-and-conditions) on Wiley Online Library for rules of use; OA articles are governed by the applicable Creative Commons License

As indicated by Martins et al. [1], broadband biophotonics applications now require the characterization of tissue optical properties from the UV to the THz domain. Journals and standards organizations should encourage permanent, citable repositories for fabrication protocols and spectral data to replace "available on request" statements.

There is also a clear opportunity to expand the range of dynamic and multilayer phantoms that reproduce physiological effects such as perfusion, oxygenation, or optical clearing [71]. Combining IAD with complementary techniques, including spatial frequency domain imaging and time-resolved spectroscopy, could provide a more robust validation framework for heterogeneous samples where traditional diffusion approximations may be limited.

Such methodological harmonization and cross-validation strategies will reinforce the role of optically characterized phantoms as quantitative reference standards, ultimately supporting safer and more reliable clinical translation of biophotonic technologies.

5 | Conclusions

Tissue mimicking phantoms characterized with the IAD method over the past decade effectively reproduce the optical regimes required for calibration and validation of modern biomedical imaging and therapeutic systems. Across PDMS, polyurethane, agar, and PVC plastisol matrices, independently tunable absorption and scattering coefficients were consistently achieved within physiological ranges of $\mu_a \approx 0.01 - 4\ \text{cm}^{-1}$ and $\mu_s' \approx 0.1 - 86\ \text{cm}^{-1}$. These ranges support reproducible reference conditions for OCT, HSI, diffuse reflectance spectroscopy, and NIRS in clinically relevant wavelength bands.

The synthesis of optical windows (Table 3), together with the scattering power-law analysis for the subset of studies reporting continuous $\mu_s'(\lambda)$ spectra (Table 4), shows that many IAD-characterized phantoms fall within the same (a, b) parameter space as representative soft tissues from Jacques [69] (Figure 2). This overlap indicates that phantom formulations can be selected or tailored not only to match target values of μ_a and μ_s' at specific wavelengths, but also to reproduce tissue-like spectral slopes. In practical terms, this provides a direct link between phantom design, tissue-equivalent optical performance, and intended clinical application.

Our findings indicate that the main barriers to cross-study comparability arise from heterogeneity in measurement configurations and the lack of standardized loss compensation, rather than fundamental limitations of the IAD method. As discussed in Section 4.2, the implementation of double integrating spheres or Monte Carlo-based corrections can substantially reduce systematic biases and improve agreement between measured and reference optical coefficients, in some cases approaching uncertainty levels below 5%. Furthermore, the statistical analysis in Section 3.6 provides a quantitative benchmark for phantom design, demonstrating that specific matrices such as PVC plastisol or gelatin–agar can be reliably tailored to match the scattering slopes (b) of target tissues such as skin or muscle. Improved reporting of fabrication protocols, explicit IAD input parameters, and fitted power-law coefficients would further strengthen reproducibility and facilitate the placement of new phantoms within standardized (a, b) design maps. Integrating these analytical refinements will expand the utility of dynamic and multilayer phantoms-including those modeling perfusion or optical clearing-for quantitative biophotonics and clinical device validation.

For clinicians and medical researchers, the present review provides a consolidated framework to identify which phantom types and optical parameter ranges are most appropriate for specific applications, such as burn-depth assessment by OCT, hyperspectral mapping of mucosal lesions, quantitative oximetry, or planning and monitoring of laser-based therapies. Overall, the evidence reviewed here shows that IAD-based optical phantom characterization is mature, robust, and well suited to support the growing need for quantitative, tissue-specific calibration standards in biomedical optics and to foster the translation of biophotonic techniques into routine clinical practice.

Author Contributions

Elvis A. García-Cortés: data curation, investigation, writing – original draft. **Luís M. Oliveira:** conceptualization, supervision, writing – review and editing. **Julio C. Pérez-Sansalvador:** conceptualization, data curation, supervision, writing – review and editing. **Teresita Spezzia-Mazzocco:** conceptualization, supervision, writing – review and editing.

Funding

This work was financed by National Funds through the Portuguese funding agency, FCT—Fundação para a Ciência e a Tecnologia, within projects LA/P/0063/2020 (DOI 10.54499/LA/P/0063/2020), UIDB/50014/2020 (DOI 10.54499/UIDB/50014/2020), and UIDP/50014/2020 (DOI 10.54499/UIDP/50014/2002). Elvis A. García-Cortés acknowledges support from a postgraduate fellowship of the Secretaría de Ciencia, Humanidades, Tecnología e Innovación (SECIHTI), Mexico (grant 923302).

Conflicts of Interest

The authors declare no conflicts of interest.

Data Availability Statement

All datasets extracted from the five studies that reported continuous $\mu_s'(\lambda)$ spectra [8, 11, 42, 67, 68] including digitized spectral points and fitted power-law parameters, are provided in the Supporting Information. No new experimental data were generated in this study.

References

1. I. S. Martins, H. F. Silva, E. N. Lazareva, et al., "Measurement of Tissue Optical Properties in a Wide Spectral Range: A Review [Invited]," *Biomedical Optics Express* 14, no. 1 (2023): 249–298.

2. S. L. Jacques, "How Tissue Optics Affect Dosimetry of Photodynamic Therapy," *Journal of Biomedical Optics* 15, no. 5 (2010): 051608.

3. A. Welch and M. van Gemert, *Optical-Thermal Response of Laser-Irradiated Tissue* (Springer Netherlands, 2011).

18640648, 2026, 4, Downloaded from https://onlinelibrary.wiley.com/doi/10.1002/jbio.70261 by Estsp Politecnico Do Porto, Wiley Online Library on [22/08/2026]. See the Terms and Conditions (https://onlinelibrary.wiley.com/terms-and-conditions) on Wiley Online Library for rules of use; OA articles are governed by the applicable Creative Commons License

4. A. N. Yaroslavsky, P. C. Schulze, I. V. Yaroslavsky, R. Schober, F. Ulrich, and H.-J. Schwarzmaier, "Optical Properties of Selected Native and Coagulated Human Brain Tissues In Vitro in the Visible and Near Infrared Spectral Range," *Physics in Medicine & Biology* 47, no. 12 (2002): 2059–2073.

5. I. J. Bigio and S. Fantini, *Quantitative Biomedical Optics: Theory, Methods, and Applications, of Cambridge Texts in Biomedical Engineering* (Cambridge University Press, 2016), Includes bibliographical references and index.

6. V. Tuchin, *Tissue Optics: Light Scattering Methods and Instruments for Medical Diagnosis*, Third ed. (SPIE, 2015).

7. P. Lemaillet, J.-P. Bouchard, J. Hwang, and D. W. Allen, "Double-Integrating-Sphere System at the National Institute of Standards and Technology in Support of Measurement Standards for the Determination of Optical Properties of Tissue-Mimicking Phantoms," *Journal of Biomedical Optics* 20, no. 12 (2015): 121310.

8. M. S. Wróbel, A. P. Popov, A. V. Bykov, V. V. Tuchin, and M. Jedrzejewska-Szczerska, "Nanoparticle-Free Tissue-Mimicking Phantoms With Intrinsic Scattering," *Biomedical Optics Express* 7, no. 6 (2016): 2088–2094.

9. R. B. Saager, A. Quach, R. A. Rowland, M. L. Baldado, and A. J. Durkin, "Low-Cost Tissue Simulating Phantoms With Adjustable Wavelength-Dependent Scattering Properties in the Visible and Infrared Ranges," *Journal of Biomedical Optics* 21, no. 6 (2016): 067001.

10. F. Ayers, A. Grant, D. Kuo, D. J. Cuccia, and A. J. Durkin, *Design and Performance Validation of Phantoms Used in Conjunction With Optical Measurements of Tissue*, ed. R. J. Nordstrom (International Society for Optics and Photonics, SPIE, 2008), 687007.

11. A. M. Goldfain, P. Lemaillet, D. W. Allen, K. A. Briggman, and J. Hwang, "Polydimethylsiloxane Tissue-Mimicking Phantoms With Tunable Optical Properties," *Journal of Biomedical Optics* 27, no. 7 (2021): 074706.

12. A. F. G. Monte, A. F. Reis, L. B. Cruz Junior, and A. Antunes, "Preparation and Quantitative Characterization of Polydimethylsiloxane Optical Phantoms With Zinc-Phthalocyanine Dye Absorbers," *Applied Optics* 57, no. 20 (2018): 5865–5871.

13. M. Nomoni, J. M. May, and P. A. Kyriacou, "Novel Polydimethylsiloxane (PDMS) Pulsatile Vascular Tissue Phantoms for the In-Vitro Investigation of Light Tissue Interaction in Photoplethysmography," *Sensors* 20 (2020): 15.

14. P. Lemaillet, J.-P. Bouchard, and D. W. Allen, "Development of Traceable Measurement of the Diffuse Optical Properties of Solid Reference Standards for Biomedical Optics at National Institute of Standards and Technology," *Applied Optics* 54, no. 19 (2015): 6118–6127.

15. C. F. Morsink, A. J. Dam-Vervloet, M. E. Krommendijk, et al., "Design and Characterization of Color Printed Polyurethane Films as Biomedical Phantom Layers," *Biomedical Optics Express* 14, no. 9 (2023): 4485–4506.

16. D. M. M. de Bruin, R. H. Bremmer, V. M. Kodach, et al., "Optical Phantoms of Varying Geometry Based on Thin Building Blocks With Controlled Optical Properties," *Journal of Biomedical Optics* 15, no. 2 (2010): 025001.

17. E.-j. Jeong, H.-W. Song, Y.-J. Lee, et al., "Fabrication and Characterization of PVCP Human Breast Tissue-Mimicking Phantom for Photoacoustic Imaging," *BioChip Journal* 11, no. 1 (2017): 67–75.

18. T. Zhang, R. Nazarov, A. P. Popov, et al., "Development of Oral Cancer Tissue-Mimicking Phantom Based on Polyvinyl Chloride Plastisol and Graphite for Terahertz Frequencies," *Journal of Biomedical Optics* 25, no. 12 (2020): 123002.

19. M. Kim, S. Im, I. Park, et al., "Fabrication of Agar-Based Tissue-Mimicking Phantom for the Technical Evaluation of Biomedical Optical Imaging Systems," *Current Applied Physics* 61 (2024): 80–85.

20. A. Paul and A. Paul, "Thermo-Mechanical Assessment of Nanoparticle Mixed Vascular Tissues Under Pulsed Ultrasound and Laser Heating," *International Journal of Thermal Sciences* 163 (2021): 106815.

21. M. Aumiller, A. Arazar, R. Sroka, O. Dietrich, and A. Rühm, "Investigations on Correlations Between Changes of Optical Tissue Properties and NMR Relaxation Times," *Photodiagnosis and Photodynamic Therapy* 45 (2024): 103968.

22. H. Durmuş and M. Seyidov, "Determination of Microscopic Optical Properties of Agar and Zerdine Phantoms at 635 nm Using Kubelka-Munk Function Approach: A Numerical Study," *International Journal of Advances in Applied Sciences* 11 (2022): 356.

23. L. Ntombela, B. Adeleye, and N. Chetty, "Low-Cost Fabrication of Optical Tissue Phantoms for Use in Biomedical Imaging," *Heliyon* 6, no. 3 (2020): e03602.

24. A. S. Kucheryavenko, I. N. Dolganova, A. A. Zhokhov, et al., "Terahertz-Wave Scattering in Tissues: Examining the Limits of the Applicability of Effective-Medium Theory," *Physical Review Applied* 20 (2023): 054050.

25. V. Virdyawan, O. Dessi, and F. Rodriguez y Baena, "A Novel Sensing Method to Detect Tissue Boundaries During Robotic Needle Insertion Based on Laser Doppler Flowmetry," *IEEE Robotics and Automation Letters* 5, no. 2 (2020): 1524–1531.

26. R. Gautam, D. Mac Mahon, G. Eager, et al., "Fabrication and Characterization of Multi-Biomarker Optimized Tissue-Mimicking Phantoms for Multi-Modal Optical Spectroscopy," *Analyst* 148 (2023): 4768–4776.

27. L. Ntombela, N. Chetty, and B. Adeleye, "Realistic Deformable Phantoms With Optical Properties of Biological Tissues for Biomedical Research Applications," *Results in Optics* 12 (2023): 100442.

28. S. Chatelin, M. Bernal, T. Deffieux, et al., "Anisotropic Polyvinyl Alcohol Hydrogel Phantom for Shear Wave Elastography in Fibrous Biological Soft Tissue: A Multimodality Characterization," *Physics in Medicine & Biology* 59, no. 22 (2014): 6923–6940.

29. E. Blumenröther, O. Melchert, M. Wollweber, and B. Roth, "Detection, Numerical Simulation and Approximate Inversion of Optoacoustic Signals Generated in Multi-Layered PVA Hydrogel Based Tissue Phantoms," *Photoacoustics* 4, no. 4 (2016): 125–132.

30. M. S. Durkee, L. D. Nash, F. Nooshabadi, J. D. Cirillo, D. J. Maitland, and K. C. Maitland, "Fabrication and Characterization of Optical Tissue Phantoms Containing Macrostructure," *JoVE* 132, no. 132 (2018): e57031.

31. S. Jenne and H. Zappe, "Multiwavelength Tissue-Mimicking Phantoms With Tunable Vessel Pulsation," *Journal of Biomedical Optics* 28, no. 4 (2023): 045003.

32. S. Monem, A. Singh, A. E. Karsten, R. Amin, and M. A. Harith, "Study of the Optical Properties of Solid Tissue Phantoms Using Single and Double Integrating Sphere Systems," *Applied Physics B* 121, no. 3 (2015): 265–274.

33. D. Fukutomi, K. Ishii, and K. Awazu, "Highly Accurate Scattering Spectra of Strongly Absorbing Samples Obtained Using an Integrating Sphere System by Considering the Angular Distribution of Diffusely Reflected Light," *Lasers in Medical Science* 30, no. 4 (2015): 1335–1340.

34. B. N. Kanakaraj and S. Narayanan Unni, "Model-Based Quantitative Optical Biopsy in Multilayer In Vitro Soft Tissue Models for Whole Field Assessment of Nonmelanoma Skin Cancer," *Journal of Medical Imaging* 5, no. 1 (2018): 014506.

35. E. E. McCabe-Lankford, T. L. Brown, and N. H. Levi-Polyachenko, "Assessing Fluorescence Detection and Effective Photothermal Therapy

18640648, 2026, 4, Downloaded from https://onlinelibrary.wiley.com/doi/10.1002/jbio.70261 by Estsp Politecnico Do Porto, Wiley Online Library on [22/08/2026]. See the Terms and Conditions (https://onlinelibrary.wiley.com/terms-and-conditions) on Wiley Online Library for rules of use; OA articles are governed by the applicable Creative Commons License

of Near-Infrared Polymer Nanoparticles Using Alginate Tissue Phantoms," *Lasers in Surgery and Medicine* 50, no. 10 (2018): 1040–1049.

36. G. M. Palmer and N. Ramanujam, "Monte Carlo-Based Inverse Model for Calculating Tissue Optical Properties Part I: Theory and Validation on Synthetic Phantoms," *Applied Optics* 45, no. 5 (2006): 1062–1071.

37. S. Schädel-Ebner, O. Hirsch, T. Gladytz, et al., "3D-Printed Tissue-Simulating Phantoms for Near-Infrared Fluorescence Imaging of Rheumatoid Diseases," *Journal of Biomedical Optics* 27, no. 7 (2022): 074702.

38. A. Kumar, G. Hattale, S. Hinge, G. Kulkarni, D. J. Late, and R. Kanawade, "Normal and Diabetic Foot Sole Skin Mimicking Tissue Phantom Fulfillment for Spectroscopic-Based DFU Diagnostics Perspective," *AIP Advances* 14, no. 6 (2024): 065014.

39. M. R. N. Avanaki, A. G. Podoleanu, M. C. Price, S. A. Corr, and S. A. Hojjatoleslami, "Two Applications of Solid Phantoms in Performance Assessment of Optical Coherence Tomography Systems," *Applied Optics* 52, no. 29 (2013): 7054–7061.

40. K.-B. Sung, K.-W. Shih, F.-W. Hsu, et al., "Accurate Extraction of Optical Properties and Top Layer Thickness of Two-Layered Mucosal Tissue Phantoms From Spatially Resolved Reflectance Spectra," *Journal of Biomedical Optics* 19, no. 7 (2014): 077002.

41. T. Li, A. Di Costanzo Mata, A. Kalyanov, M. Wolf, and J. Jiang, "Fabrication of Tuneable Tissue-Mimicking Phantom for Optical Methods," in *Oxygen Transport to Tissue XLV*, ed. K. Sakatani, K. Masamoto, Y. Yamada, F. Scholkmann, and J. C. LaManna (Springer International Publishing, 2024), 239–243.

42. V. D. Vincely and K. Vishwanath, "Accuracy of Retrieving Optical Properties From Liquid Tissue Phantoms Using a Single Integrating Sphere," *Applied Optics* 61, no. 2 (2022): 375–385.

43. A. Pacheco, K. Grygoryev, W. Messina, and S. Andersson-Engels, "Lung Tissue Phantom Mimicking Pulmonary Optical Properties, Relative Humidity, and Temperature: A Tool to Analyze the Changes in Oxygen Gas Absorption for Different Inflated Volumes," *Journal of Biomedical Optics* 27, no. 7 (2021): 074707.

44. G. Liu, K. Huang, Q. Jia, et al., "Fabrication of a Multilayer Tissue-Mimicking Phantom With Tunable Optical Properties to Simulate Vascular Oxygenation and Perfusion for Optical Imaging Technology," *Applied Optics* 57, no. 23 (2018): 6772–6780.

45. C. Chen, F. Klämpfl, C. Knipfer, et al., "Preparation of a Skin Equivalent Phantom With Interior Micron-Scale Vessel Structures for Optical Imaging Experiments," *Biomedical Optics Express* 5, no. 9 (2014): 3140–3149.

46. A. Kumar, G. Hattale, D. Pawar, and R. Kanawade, "Fabrication and Evaluation of a Spatially Resolved Fiber-Optic Probe for Diffuse Reflectance Measurement for Noninvasive Diabetic Foot Ulcer Diagnosis Perspective," *Optical Engineering* 63, no. 4 (2024): 044103.

47. T. Li, A. Kalyanov, M. Wolf, et al., *Oxygen Transport to Tissue XLIV*, ed. F. Scholkmann, J. LaManna, and U. Wolf (Springer International Publishing, 2023), 179–183.

48. B. A. Bright, V. Damodaran, and T. Jayanthi, "Design of Eye Phantom for Optical Coherence Tomography Angiography Study," *International Journal of Artificial Organs* 47, no. 12 (2024): 920–927.

49. S. A. Prahl, M. J. C. van Gemert, and A. J. Welch, "Determining the Optical Properties of Turbid Media by Using the Adding–Doubling Method," *Applied Optics* 32, no. 4 (1993): 559–568.

50. P. Lemaillet, C. C. Cooksey, J. Hwang, et al., "Correction of an Adding-Doubling Inversion Algorithm for the Measurement of the Optical Parameters of Turbid Media," *Biomedical Optics Express* 9, no. 1 (2018): 55–71.

51. A. A. Song, M. T. Chen, T. L. Bobrow, and N. J. Durr, "Speckle-Illumination Spatial Frequency Domain Imaging With a Stereo Laparoscope for Profile-Corrected Optical Property Mapping," *Journal of Biomedical Optics* 30, no. S1 (2025): S13710.

52. A. C. M. Mendes, A. F. G. Monte, and R. B. Saager, "Innovative Methodology for Noninvasive Spatial Mapping of Gold Nanoparticle Distribution in Tissues: Potential Applications in Biomedical Imaging and Therapy," *Journal of the Optical Society of America. A* 41, no. 7 (2024): 1337–1346.

53. J. Crowley and G. S. D. Gordon, "Ultra-Miniature Dual-Wavelength Spatial Frequency Domain Imaging for Micro-Endoscopy," *Journal of Biomedical Optics* 29, no. 2 (2024): 026002.

54. Y. Feng, C. Cao, Y. Shimada, et al., "Motion-Resistant Three-Wavelength Spatial Frequency Domain Imaging System With Ambient Light Suppression Using an 8-Tap CMOS Image Sensor," *Journal of Biomedical Optics* 29, no. 1 (2024): 016006.

55. D. Milej, A. Abdalmalak, D. Janusek, M. Diop, A. Liebert, and K. S. Lawrence, "Time-Resolved Subtraction Method for Measuring Optical Properties of Turbid Media," *Applied Optics* 55, no. 7 (2016): 1507–1513.

56. Z. Nie, V. N. Du Le, D. Cappon, et al., "Integrated Time-Resolved Fluorescence and Diffuse Reflectance Spectroscopy Instrument for Intraoperative Detection of Brain Tumor Margin," *IEEE Journal of Selected Topics in Quantum Electronics* 22, no. 3 (2016): 49–57.

57. K. Erdenedalai, R. Maltais-Tariant, M. Dehaes, and C. Boudoux, "MCOCT: An Experimentally and Numerically Validated, Open-Source Monte Carlo Simulator for Optical Coherence Tomography," *Biomedical Optics Express* 15, no. 2 (2024): 624–640.

58. L. Waszczuk, J. Ogien, F. Pain, and A. Dubois, "Determination of Scattering Coefficient and Scattering Anisotropy Factor of Tissue-Mimicking Phantoms Using Line-Field Confocal Optical Coherence Tomography (LC-OCT)," *Journal of the European Optical Society-Rapid Publications* 19 (2023): 2.

59. I. Saytashev, Y.-C. Yoon, B. J. Vakoc, S. Vasudevan, and D. X. Hammer, "Improved In Vivo Optical Coherence Tomography Imaging of Animal Peripheral Nerves Using a Prism Nerve Holder," *Journal of Biomedical Optics* 28, no. 2 (2023): 026002.

60. N. Rein, R. Shechter, E. Tsizin, et al., "Optical Anchor Bolt for Simultaneous Stereo-EEG and Intracranial Functional Near Infrared Spectroscopy: Concept, Phantom Experiment, and Monte Carlo Simulation," *IEEE Sensors Journal* 25, no. 1 (2025): 1359–1371.

61. P. S. Saha, J. Yan, and C. Zhu, "Diffuse Reflectance Spectroscopy for Optical Characterizations of Orthotopic Head and Neck Cancer Models In Vivo," *Biomedical Optics Express* 15, no. 7 (2024): 4176–4189.

62. A. Tzroya, H. Duadi, and D. Fixler, "Extracting Superficial Scattering by Q-Sensing Technique," *Journal of Biophotonics* 18 (2024): e202400262.

63. J. Stergar, R. Hren, and M. Milanič, "Effects of Phantom Microstructure on Their Optical Properties," *Journal of Biomedical Optics* 29, no. 9 (2024): 093502.

64. M. R. Pinheiro, M. I. Carvalho, and L. M. Oliveira, "Tutorial on the Use of the Photon Diffusion Approximation for Fast Calculation of Tissue Optical Properties," *Journal of Biophotonics* 18 (2024): e202400257.

65. M. J. Page, J. E. McKenzie, P. M. Bossuyt, et al., "The PRISMA 2020 Statement: An Updated Guideline for Reporting Systematic Reviews," *BMJ (Clinical Research Edition)* 372 (2021): n71.

66. H. Jang, T. J. Pfefer, and Y. Chen, "Solid Hemoglobin-Polymer Phantoms for Evaluation of Biophotonic Systems," *Optics Letters* 40, no. 18 (2015): 4321–4324.

67. H. Kim, N. T. Hau, Y.-G. Chae, B.-i. Lee, and H. W. Kang, "3D Printing-Assisted Fabrication of Double-Layered Optical Tissue Phantoms for Laser Tattoo Treatments," *Lasers in Surgery and Medicine* 48, no. 4 (2016): 392–399.

18640648, 2026, 4, Downloaded from https://onlinelibrary.wiley.com/doi/10.1002/jbio.70261 by Estsp Politecnico Do Porto, Wiley Online Library on [22/08/2026]. See the Terms and Conditions (https://onlinelibrary.wiley.com/terms-and-conditions) on Wiley Online Library for rules of use; OA articles are governed by the applicable Creative Commons License

68. M. S. Wróbel, A. P. Popov, A. V. Bykov, M. Kinnunen, M. Jedrzejewska-Szczerska, and V. V. Tuchin, "Measurements of Fundamental Properties of Homogeneous Tissue Phantoms," *Journal of Biomedical Optics* 20, no. 4 (2015): 045004.

69. S. L. Jacques, "Optical Properties of Biological Tissues: A Review," *Physics in Medicine and Biology* 58, no. 11 (2013): R37.

70. J. Dinh, A. Yamashita, H. Kang, S. Gioux, and H. S. Choi, "Optical Tissue Phantoms for Quantitative Evaluation of Surgical Imaging Devices," *Advanced Photonics Research* 4, no. 1 (2023): 2200194.

71. L. R. Oliveira, M. R. Pinheiro, D. K. Tuchina, P. A. Timoshina, M. I. Carvalho, and L. M. Oliveira, "Light in Evaluation of Molecular Diffusion in Tissues: Discrimination of Pathologies," *Advanced Drug Delivery Reviews* 212 (2024): 115420.

Supporting Information

Additional supporting information can be found online in the Supporting Information section. **Data S1:** It includes: search strategies for all databases, digitized reduced-scattering spectra from five studies, and fitted power-law parameters used in the analysis.

18640648, 2026, 4, Downloaded from https://onlinelibrary.wiley.com/doi/10.1002/jbio.70261 by Estsp Politecnico Do Porto, Wiley Online Library on [22/08/2026]. See the Terms and Conditions (https://onlinelibrary.wiley.com/terms-and-conditions) on Wiley Online Library for rules of use; OA articles are governed by the applicable Creative Commons License